Carrier Density and Delocalization Signatures in Doped Carbon Nanotubes from Quantitative Magnetic Resonance

Supporting Information

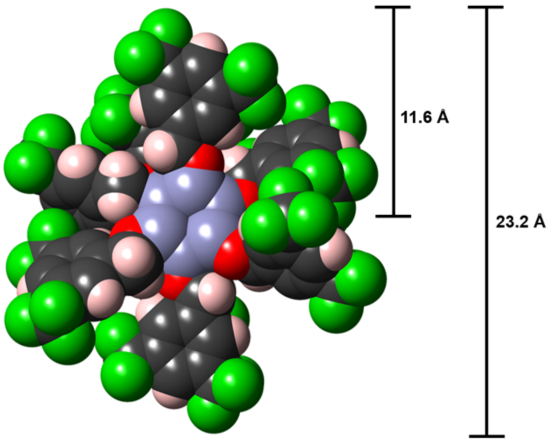

Figure S1. Dodecaborane clusters substituted with fluorinated aryl groups depicting van Der Waals radius and distance from the center of boron cluster to outer van Der Waals radius.

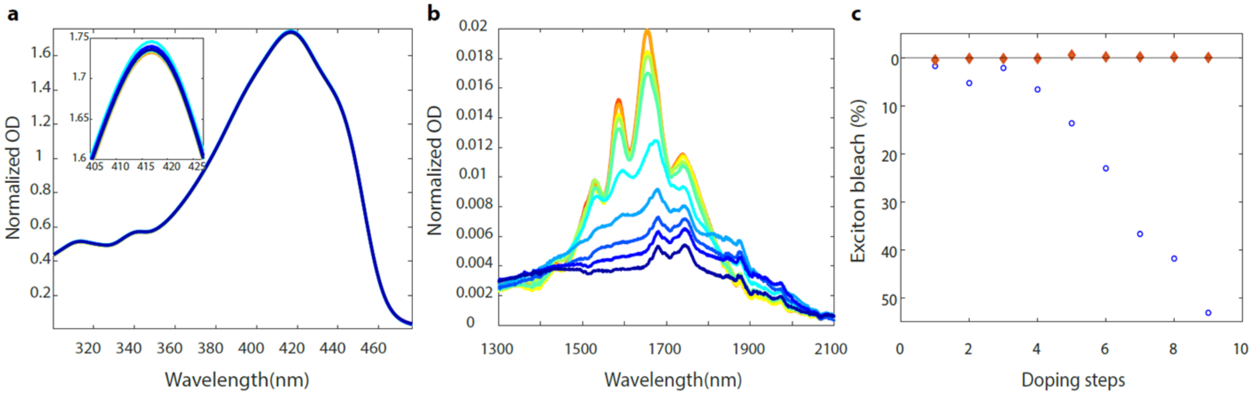

Figure S2. Polymer control doping experiments: a) Polymer (PF-PD) excitonic transition with indistinguishable exciton bleaching, b) s-SWCNTs S_{11} excitonic transition showing complete bleaching and c) exciton bleach calculated for the polymer (orange diamonds) with undistinguishable bleaching compared to SWCNTs (blue circles) bleaching as a function of increasing doping steps.

PLE map experiments

From the ^{19}F NMR measurements, DDB-F72 anion concentrations are calculated. To accurately calculate the charge density per nm of s-SWCNTs, PLE map measurements were performed to identify the chiralities present in our dispersion. Different chiralities have different diameters, and the relationship between diameter and # number of carbon atoms per nm is diameter dependent. In Figure S3 we present the experimental PLE map (S3a) together with the fitted simulation (S3b) with the identified chiralities. We also present slices for emission spectra (Figure S3c) and excitation spectra (Figure S3d) showing experimental data (black curve) with the simulated data (red curve) showing good agreement. PLE fits were obtained with a previously developed empirical 2D fitting model that considers both excitonic and band-to-band transitions in the excitation profile and is described in more detail in the work done by Campo *et. al*[3]. The identified chiralities and corresponding fitted PL intensities are plotted in Figure S4. Based on this chirality PL intensity distribution, we calculated the number of carbon atoms, and then converted into a length in nm to obtain charge density per nm.

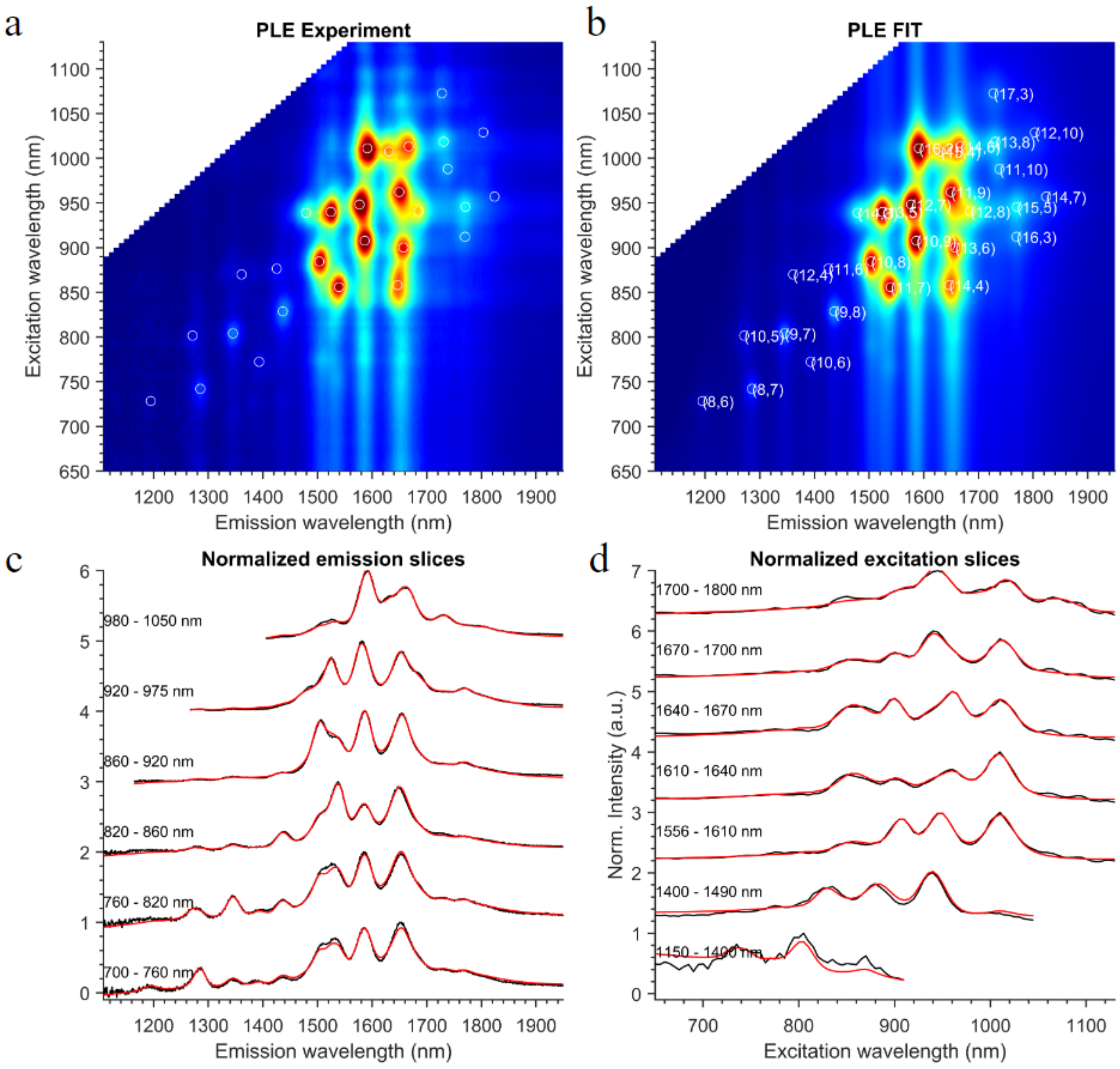

Figure S3. a) PLE experimental map of the s-SWCNTs, undoped. b) Fitted PLE map to identify chiralities present in the SWCNT dispersion. Labels show specific chiralities fitted for specific PLE peaks. c) Normalized emission spectrum slices at different excitation wavelength regions (refer to panel a). d) Normalized excitation spectra slice for different emission wavelength regions (refer to panel a). Black lines represent the experimental data, and the red curve is the fitted simulation for the identified chiralities.

The list of identified chiralities can be obtained from Figure S4 and S5: (10,8), (14,3), (11,7), (13,5), (14,4), (10,9), (12,7), (13,6), (16,2), (11,9), (15,4), (12,8), (16,3), (14,6), (15,5), (11,10), (13,8), (14,7), (17,3), (12,10). Figure S4 shows the chiralities as a function of diameter and Figure S5 presents a color map of the chiralities and corresponding PLE intensity.

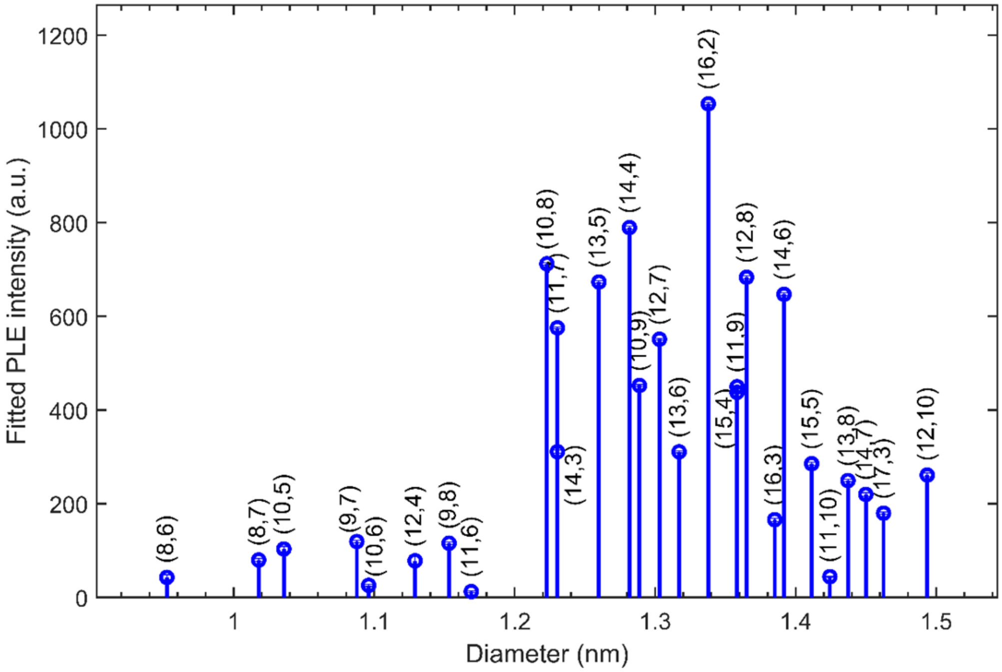

Figure S4. Chiralities identified from PLE map fitting and corresponding fitted PLE intensities.

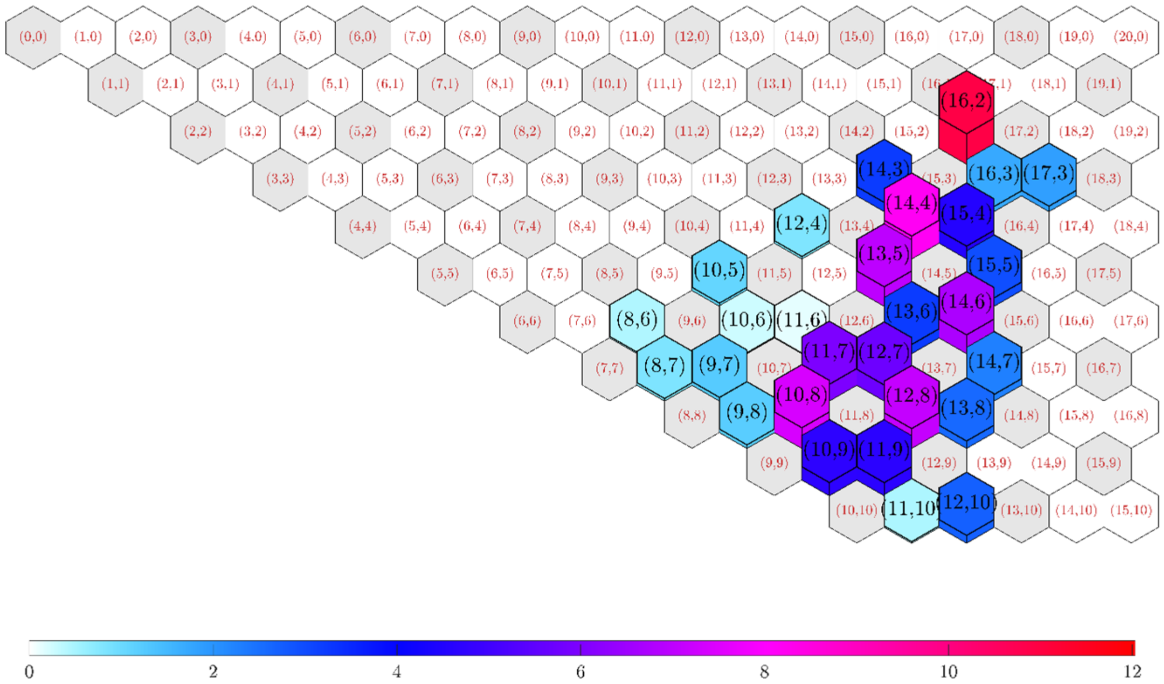

Figure S5. Color map for chiralities identified and PL intensities, providing an indicator of the chiral abundances, though not considering PL quantum efficiencies. Chiralities in red letters were not included in the fit.

NMR control experiments

As mentioned in the main text, we performed control NMR experiments, a polymer doping series, shown in Figure S6. Compared to the s-SWCNTs dispersion, the polymer doping series does not present the peak shift observed as DDB-F72 concentration increases. NMR linewidth broadening increases and new features are observed after 10 µM of DDB-F72 (first light blue spectrum). Broadening of the NMR signal can be a consequence of DDB-F72 doping the polymer or aggregation[4] on the DDB-F72, which is known to occur for high concentration. NMR spectra are arbitrarily displaced along the y axis for better comparison.

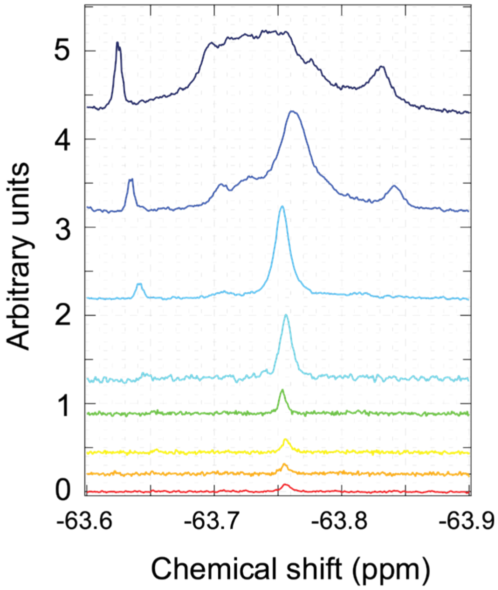

Figure S6. Polymer PFPD doping series. NMR signal does not shift as DDB-F72 concentration increases, but broadening and new features appear as a result of dopant aggregation at high concentrations. Doping series concentrations: 0.95 µM, 1.5 µM, 2.1 µM, 3.8 µM, 11 µM, 20 µM, 41 µM and 88 µM.

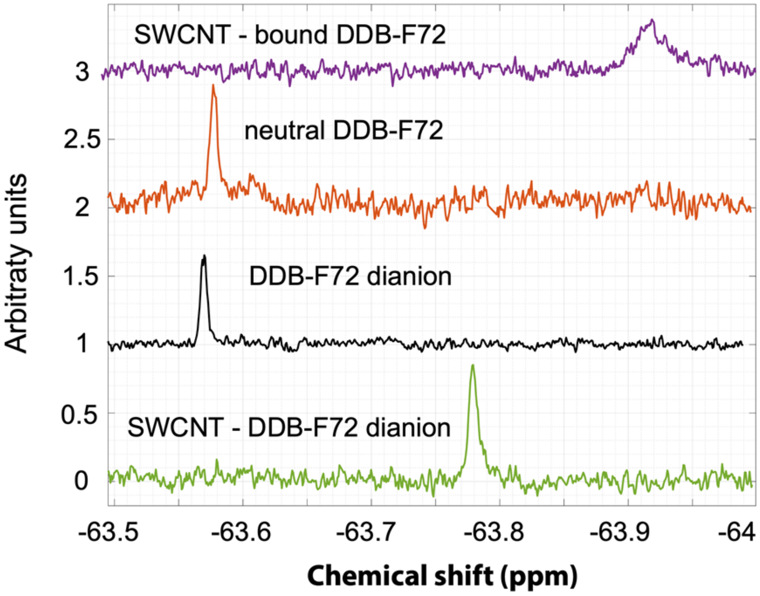

Figure S7. Control NMR experiments showing chemical shift due to DDB-F72 bound to SWCNTs as a result of charge transfer. Neutral DDB-F72 in d8-toluene is shown in the orange curve, and the dianion, DDB-F2$^-$, is the black spectrum showing a small difference in chemical shift compared to the neutral dopant. The purple spectrum corresponds to the SWCNTs dispersion with added neutral DDB-F72 that can inject a hole (undergo charge transfer) with a considerable chemical shift with respect to both neutral and dianion DDB-F72, in addition to signal broadening due to bound nature of dopant. The green spectrum corresponds to the SWCNTs dispersion with doubly reduced DDB-F72, no charge injection can occur in this redox state. The chemical shift is different to the bound DDB-F72 dopant, narrow linewidth is observed.

Phase-space filling model

For complete background derivation of the phase-space model used here, please refer to work by Eckstein, et al[5]. We begin by calculating the carrier density as a function of the Fermi level, E_F, from the density of states (DOS). We started with the DFT-calculated DOS of the representative (10,8) chirality shown in Figure 1 in the main text, where the DOS is represented by $g(E)$ in equation 1, and the Fermi-Dirac distribution, $f(E,T)$. For full DFT calculations please refer to the work by Avery, *et al*.[6]

$$n = \int g(E) f(E,T) dE \tag{1}$$

The carrier density then can be defined as

$$n\left(E_F, T\right) = \frac{4}{\pi}\int_0^{\infty} f_e\left(k,E_F,T\right) dk \tag{2}$$

And the exciton bleaching can be calculated from the following expression numerically.

$$\chi\left(E_F,T\right) = 2c^{-1}\int_0^{\infty} f_e\left(k,E_F,T\right) \Psi(k)\, dk \tag{3}$$

And the wavefunction is defined as

$$\Psi(k) = 2^{0.5}\xi^{0.5}\pi^{0.25}e^{-\frac{k^2\xi^2}{2}} \tag{4}$$

$$c = \int_{-\infty}^{\infty} \Psi(k) dk = 2\xi^{-0.5}\pi^{0.75} \tag{5}$$

It is worth noting that if the DOS is derived in energy, then the above equations must have a variable change and the corresponding Jacobian must be added.

$$dk = \sqrt{\frac{m}{2E\hbar^2}}\, dE \tag{6}$$

To determine the best parameters for our s-SWCNTs dispersion, we created a matrix with different effective mass values ranging from 0.05m_e to 0.14m_e and exciton size values ranging from 2 nm to 13 nm. We thus present different combinations, but not the complete set, in the different steps that require it. The carrier density and exciton bleach must be numerically calculated separately. The Jacobian for different effective mass values is shown in Figure S8a. Equation 2, before numerical evaluation is shown in Figure S8b.

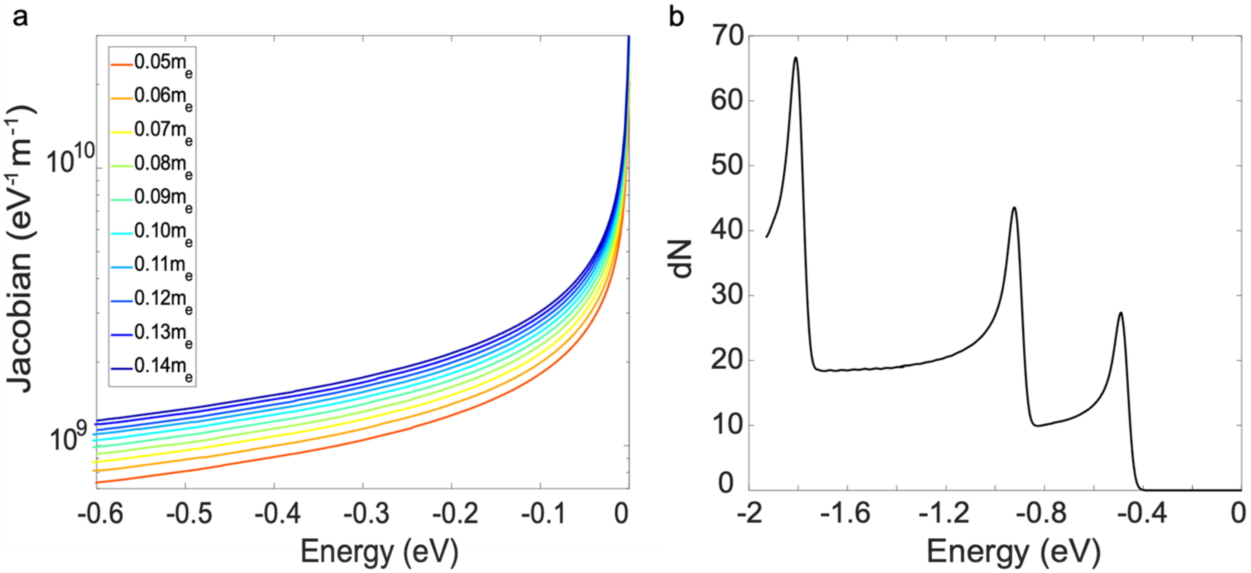

Figure S8. a) Jacobian calculated for ten different effective mass values to correct for DOS in energy, compared to k space. b) Expression for carrier density before numerical integration (dN) as a function of energy.

Wavefunctions plotted in Figure S9 are not normalized, normalization is performed at the last step when plotting carrier density versus exciton bleaching.

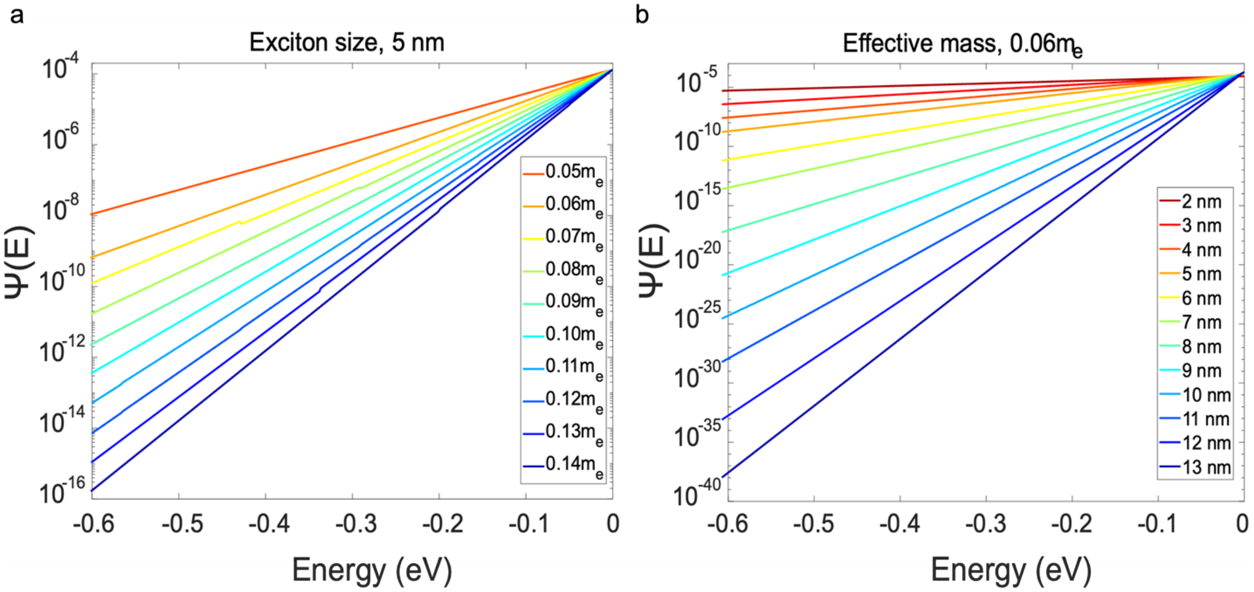

Figure S9. a) Wavefunction calculated from equation 4 for different effective mass values, at constant exciton size, 5nm. b) Wavefunction calculated from equation 4 for different exciton size values, at constant effective mass, 0.06m_e. Wavefunctions are not normalized.

Numerically evaluated integrals of equation 2 and equation 3 are shown in Figure S10, where four different exciton size are shown for varying effective mass values.

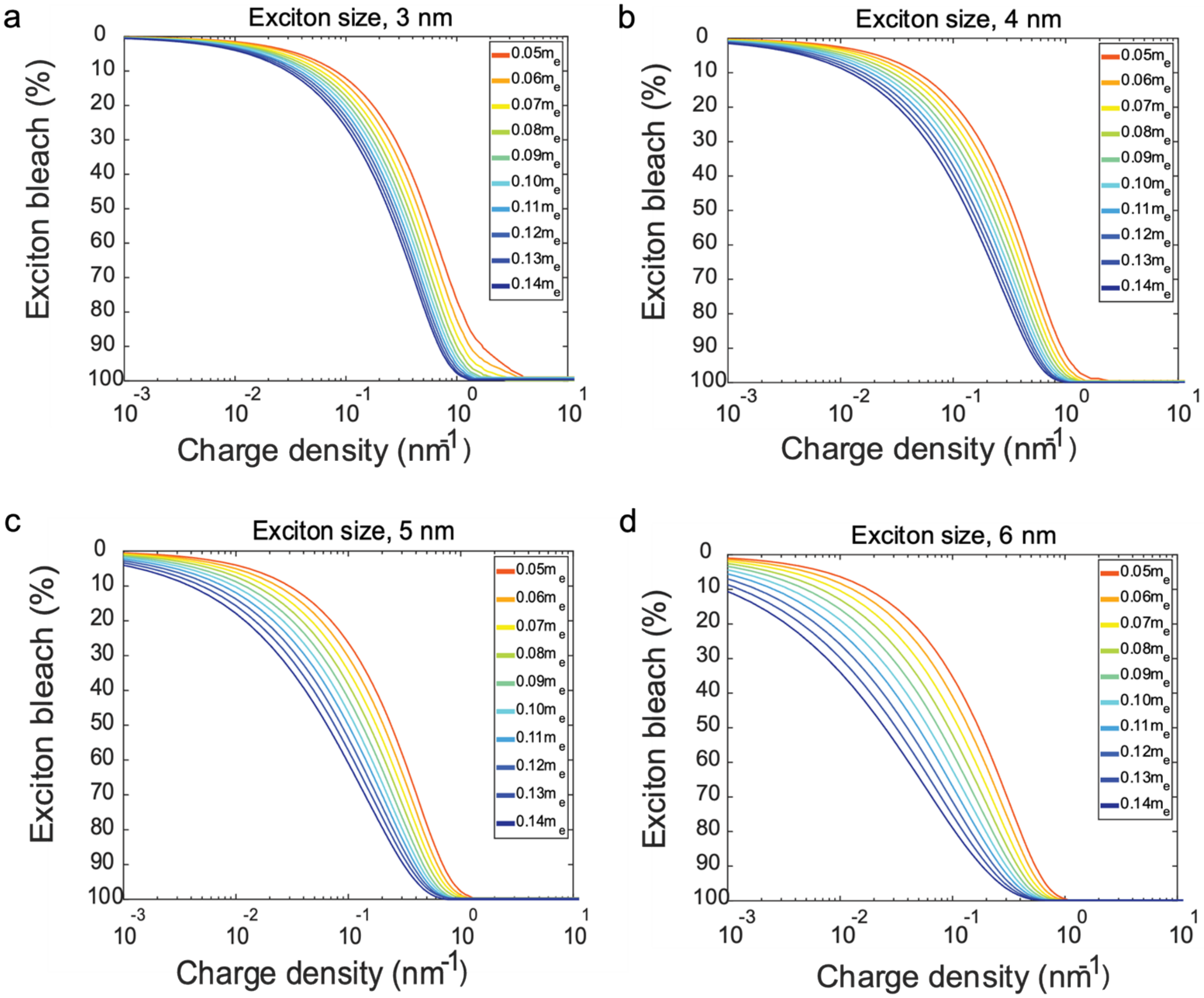

Figure S10. Exciton bleach calculated from equation 3 versus charge density calculated from equation 2 after numerical integration for a) 3nm, b) 4 nm, c) 5 nm and d) 6 nm exciton size for varying effective mass values.

Numerically evaluated integrals of equation 2 and equation 3 are shown in Figure S11, where four different effective mass values are shown for varying exciton size values.

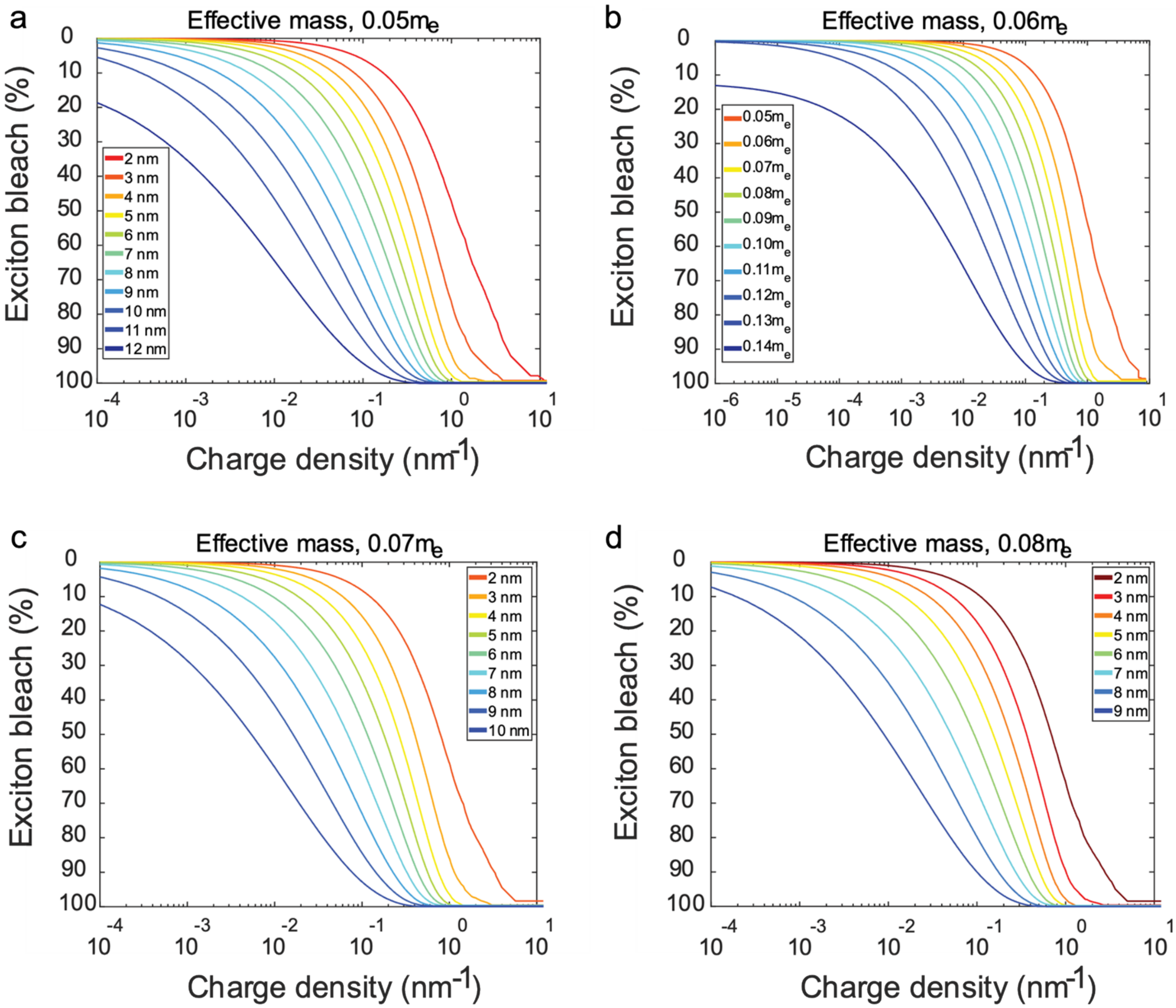

Figure S11. Exciton bleach calculated from equation 3 versus charge density calculated from equation 2 after numerical integration for a) 0.05m_e, b) 0.06m_e, c) 0.07m_e and d) 0.08m_e exciton size for varying exciton size values.

Three additional calculated DOS of different diameter were also analyzed (16,0), (17,0) and (19,0) to find the best fit for the experimental data and represent the current diameter distribution. The best fit was found for (10,8) chirality and this is the data set presented here.

Exciton bleach correction

The exciton bleach was corrected to remove the contribution from the trion for the total area under the absorption curve (Figure 1a). This correction was done based on the calibration curve presented in Figure S12, showing the ratio between area of the trion and total area (trion+S_{11} exciton) as a function of total area. For each calculated ground state bleach from steady state absorption, the corresponding trion area contribution was removed. The corrected data shifts to larger exciton bleach because the trion contributes to the total area, resulting in smaller S_{11} exitonic bleaching, i.e., as doping increases the S_{11} transition decreases but the trion intensity increases. The experimental data to obtain the calibration curve is found on the work by Eckstein, *et al*[5]. A single chirality is used because this prevents the overlap of S_{11} exciton and trion, X^+ to produce a reliable calibration curve. In Figure S11 the ratio between the trion area to the total area is correlated to the bleach calculated from the experimental (uncorrected) data. The fit can be found in equation 7, where x is the bleach.

$$\frac{A_{X^+}}{A_{S_{11}+X^+}} = \frac{0.40112 \pm 0.0103}{1 + \left(\frac{0.1987 \pm 0.00575}{x}\right)^{2.7891 \pm 0.157}} \tag{7}$$

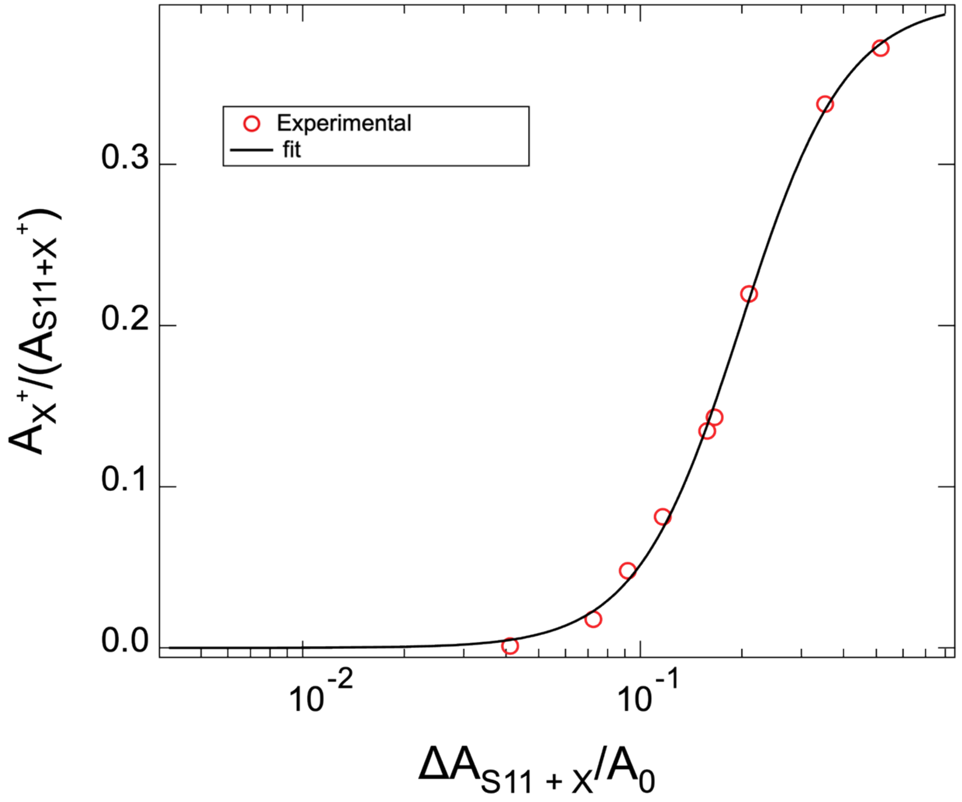

Figure S12. Area ratio (Trion area/Trion+S_{11} area) as a function of bleach Trion+S_{11}. Experimental is represented by red circles and fit (black line). Calibration curve to determine trion area contribution to total area under absorption curve to correct exciton bleach.

For every doping level, the exciton bleaching is calculated from 1400 to 2100 nm range. This range includes S_{11} and X^+ contributions. The excitonic bleaching is the independent variable in equation 7, used to determine the contribution of the trion to the total area. Subtracting the trion contribution results in a corrected area that is then used to calculate the new excitonic bleaching.

References

(1) Lei, T.; Chen, X.; Pitner, G.; Wong, H.-S. P.; Bao, Z. Removable and Recyclable Conjugated Polymers for Highly Selective and High-Yield Dispersion and Release of Low-Cost Carbon Nanotubes. *J. Am. Chem. Soc.* **2016**, *138* (3), 802–805. https://doi.org/10.1021/jacs.5b12797.

(2) Aubry, T. J.; Axtell, J. C.; Basile, V. M.; Winchell, K. J.; Lindemuth, J. R.; Porter, T. M.; Liu, J.-Y.; Alexandrova, A. N.; Kubiak, C. P.; Tolbert, S. H.; Spokoyny, A. M.; Schwartz, B. J. Dodecaborane-Based Dopants Designed to Shield Anion Electrostatics Lead to Increased Carrier Mobility in a Doped Conjugated Polymer. *Adv. Mater.* **2019**, No. 31, 1805647. https://doi.org/10.1002/adma.201805647.

(3) Campo, J.; Cambré, S.; Botka, B.; Obrzut, J.; Wenseleers, W.; Fagan, J. A. Optical Property Tuning of Single-Wall Carbon Nanotubes by Endohedral Encapsulation of a Wide Variety of Dielectric Molecules. *ACS Nano* **2021**, *15* (2), 2301–2317. https://doi.org/10.1021/acsnano.0c08352.

(4) Mashiach, R.; Weissman, H.; Avram, L.; Houben, L.; Brontvein, O.; Lavie, A.; Arunachalam, V.; Leskes, M.; Rybtchinski, B.; Bar-Shir, A. In Situ NMR Reveals Real-Time Nanocrystal Growth Evolution via Monomer-Attachment or Particle-Coalescence. *Nat. Commun.* **2021**, *12* (1), 229. https://doi.org/10.1038/s41467-020-20512-6.

(5) Eckstein, K. H.; Oberndorfer, F.; Achsnich, M. M.; Schöppler, F.; Hertel, T. Quantifying Doping Levels in Carbon Nanotubes by Optical Spectroscopy. *J. Phys. Chem. C* **2019**, *123* (49), 30001–30006. https://doi.org/10.1021/acs.jpcc.9b08663.

(6) Avery, A. D.; Zhou, B. H.; Lee, J.; Lee, E.-S.; Miller, E. M.; Ihly, R.; Wesenberg, D.; Mistry, K. S.; Guillot, S. L.; Zink, B. L.; Kim, Y.-H.; Blackburn, J. L.; Ferguson, A. J. Tailored Semiconducting Carbon Nanotube Networks with Enhanced Thermoelectric Properties. *Nat. Energy* **2016**, *1* (4), 16033. https://doi.org/10.1038/nenergy.2016.33.